



CHORUS

This is the accepted manuscript made available via CHORUS. The article has been published as:

Chiral Topological Surface States on a Finite Square Photonic Crystal Bounded by Air

Anna C. Tasolamprou, Maria Kafesaki, Costas M. Soukoulis, Eleftherios N. Economou, and
Thomas Koschny

Phys. Rev. Applied **16**, 044011 — Published 11 October 2021

DOI: [10.1103/PhysRevApplied.16.044011](https://doi.org/10.1103/PhysRevApplied.16.044011)

Chiral topological surface states on a finite square photonic crystal bounded by air

Anna C. Tasolamprou,^{1,*} Maria Kafesaki,^{1,2} Costas M. Soukoulis,^{1,3} Eleftherios N. Economou,^{1,4} and Thomas Koschny³

¹*Institute of Electronic Structure and Laser, Foundation for Research and Technology Hellas, N. Plastira 100, 70013 Heraklion, Crete, Greece*

²*Department of Materials Science and Technology, University of Crete, Heraklion, 70013, Greece*

³*Ames Laboratory and Department of Physics and Astronomy, Iowa State University, Ames, Iowa 50011, USA*

⁴*Department of Physics, University of Crete, Heraklion, Greece*

Chiral, topologically protected, photonic surface states can be found at the boundary between gyrotropic photonic crystals where a changing magnetic field induces different topology across the interface. Typically, either photonic crystals with suitable band structure are required on both sides of the interface to provide a bandgap and evanescent decay of the surface states away from the interface on both sides or an outer layer with engineered material properties. In this paper we show the emergence of topological, unidirectional surface states at the termination of finite gyrotropic photonic crystals with simple square lattice and C^4 rotational symmetry bounded by vacuum, eliminating the need for an outside layer to enable chiral surface modes. We start from an infinite, time-reversal-symmetry-breaking photonic crystal with a bandgap associated with bands with non-zero Chern numbers, different from all-zero Chern numbers in air. We then modify the photonic crystal to move this gap below the lightline, while maintaining the Chern number discontinuities. Band structure calculations for a supercell approximating a photonic crystal finite in the direction normal to the surface demonstrate the existence, dispersion, and chirality of the surface mode. Extensive direct scattering calculations of a point source and spatial Fourier analysis, further reveal a unidirectional free space topological surface state, which propagates anticlockwise around the surface of a finite photonic crystal, providing a nearly foolproof way to cross-check the surface mode band structure unaffected by back-scattering from local defects. Additionally, scattering simulations allow for an independent characterization of the state dispersion and unveil the robustness of the topological plasmonic mode propagation around the 90° bends of the structure, being accountable only to radiation leakage. In contrast to buried topological surface states, the observed surface modes at the photonic crystal-air interface have the advantage of being accessible to the outside world allowing to take advantage of the defect tolerant back-scattering-free surface modes to engineer emission from photonic crystal surfaces into arbitrary free space beam shapes and directions.

Keywords: topological photonics, photonic crystals, gyrotropic photonic crystals, topological surface states, magneto-plasmons, topological plasmons, unidirectional propagation, back-scattering immunity

I. INTRODUCTION

Topological insulators are solid-state materials that exhibit an insulating behavior in the bulk while supporting the transport of electrons along their surface without any back-scattering and dissipation, mostly unperturbed by defects and impurities [1]. The topological effects observed in solid-state physics have been translated in photonics early in the present century [2], opening the path to the realization of exciting phenomena and photonic devices [3–7], which can avoid the generally unwanted back-reflection and loss that pose critical constraints in photonic circuits. Because of their unmatched versatility in engineering the photonic band structure, inevitably, it was proven that photonic crystals would play a leading role in realizing topological photonic systems. Photonic crystals are periodic structures, with lattice constants comparable to the wavelength of operation, that allow or prohibit the propagation of electromagnetic waves of

selected frequency, polarization, and traveling direction in the interior, thus, opening photonic bandgaps, much like the electronic bandgaps of a solid-state semiconductor material [8]. Engineering the photonic crystal bandgap has enabled the electromagnetic wave manipulation, the localization, waveguiding, and resonant response in one, two, or three dimensional systems, operating across the vast electromagnetic spectrum [9–12]. In 2008 it was shown that photonic crystals made of materials with time-reversal-symmetry-breaking Faraday-effect sustain chiral edge modes that propagate unidirectionally along boundaries across which the Faraday axis reverses, unaffected from defects and disorder [13–16], constituting the photonic analog of the electronic edge states appearing in quantum-Hall-effect systems [17]. The initial observations attracted great scientific attention and prompted a large number of theoretical and experimental works investigating the features of topological surface states appearing at the interfaces of topologically non-trivial media [16, 18–23]. More recent investigations revealed that photonic non-trivial topology can exist at all dielectric interfaces with properly deformed lattices of hexagonal symmetry [24–27] as well as in more com-

* atasolam@iesl.forth.gr

plex and experimentally challenging systems comprising broken Hermiticity [28–31].

In the vast majority of the related investigations, topological effects are investigated at the interfaces between photonic crystals, trivial or non-trivial, and another medium that presents a bandgap or properly engineered dispersion. However, truncated photonic crystals have been shown to sustain the propagation of trivial bound states at their interfaces with free space [32–37], much like a surface plasmon polariton [38], while one-way free-space surface states have been reported in honeycomb magneto-optical photonic crystals [39, 40]. The discussion in explicitly free space terminated photonic crystals topological surface states mainly involves lattices with hexagonal rotational symmetry. A dipole model involving atoms of three dimensional point scatterers, again in a honeycomb lattice [41], and a hexagonal crystal with antichiral edge states, have recently been shown to sustain free-space topological surface modes [42, 43]. Other approaches to achieve free-space topological surface modes involve gyromagnetic, hyperbolic metamaterials [44], zig-zag disk chains, and other hexagonal lattices variants [45–48], including graphene enabled topological plasmons [49].

In this work we present the study of a comparatively much more simple, realistic, and experimentally accessible photonic crystal with square lattice and C^4 rotational symmetry (different than the most investigated hexagonal crystals of C^6 rotational symmetry) that, under properly adjusted filling ratio, sustains topological, unidirectional surface modes at the interfaces with the surrounding free space (air or vacuum), eliminating the need for an outside photonic crystal covering to enable chiral topological surface modes. The occurrence of topological surface states at the interface to air greatly improves their accessibility and can prove very useful for interconnects and out-coupling in photonic circuits, applying also as antenna arrays [50]. As with topological surface states at the internal interface between photonic crystals of different topology, the topological surface mode appears in the spectral regime between bands presenting a change in the sum of Chern numbers of the bands below, across the interface. We begin our investigation from the dispersion diagrams of the infinite photonic crystal and modify its geometry to bring the bandgap that supports emerging topological states below the lightline. We then calculate the dispersion properties of the topological plasmonic modes by utilizing a supercell approach and we finally demonstrate the one-way directionality of the mode by explicitly exciting a truncated photonic crystal square structure with a dipole source. The dispersion of the unidirectional topological surface state is demonstrated independently, both from the eigenmode solutions for the supercell band structure as well as from the Fourier analysis of the surface fields excited by a suitable point source in the direct scattering simulation in frequency domain. With the scattering simulations we also quantify the back-scattering free nature of the topological mode

and the robustness of the propagation in the corners of the structure, i.e. the 90° bends, where due to the free space interface, unavoidable radiation losses but no back-scattering in the surface mode occur.

II. UNIT CELL AND SUPERCELL BAND STRUCTURE

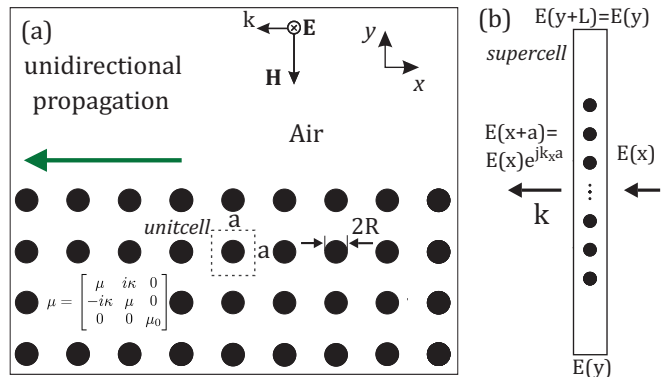


FIG. 1. (a) Schematic of the gyrotropical crystal and air interface that sustains the free space topological surface states. The photonic crystal half space consists of a two dimensional, square lattice of magneto-optical circular rods, infinite in the vertical direction z , with radius R and lattice constant a . The electric field is polarized along the rods axis $\mathbf{E} = E \mathbf{e}_z$. (b) Schematic of the supercell of height L , consisting of a finite structure along the y padded with air and periodic along the x direction, and boundary conditions for calculating the dispersion of the surface mode in the finite photonic crystal.

Let us first consider the (bulk) band structure and topological properties of the infinite photonic crystal. The schematic layout of the photonic crystal/air interface and the geometry of the supercell used to obtain the band structure of the surface states are illustrated in Fig. 1. The system consists of a two dimensional, rectangular, magneto-optical photonic crystal, made of infinitely long cylinders with radius R and lattice constant a . The polarization of the field is assumed to be along the long axis of the cylinders, $\mathbf{E} = E \mathbf{e}_z$. The cylinders are made a gyrotropic material, Yttrium-Iron-Garnet (YIG), subject to an external magnetic field along their axis direction. YIG is a ferrimagnetic material that exhibits magnetic behavior in microwaves [51] and has been extensively studied as a constituent material for topological photonic crystals. This material’s strong gyromagnetic anisotropy under an external magnetic field is described by a non-diagonal permeability tensor,

$$\mu = \begin{bmatrix} \mu & i\chi & 0 \\ -i\chi & \mu & 0 \\ 0 & 0 & \mu_0 \end{bmatrix}, \quad (1)$$

which enforces the time-reversal-symmetry breaking of the photonic crystal. Changing the direction of the external field allows to easily modify the sign of the topology

or turn it off all together (by controlling the off-diagonal elements in the permeability tensor). In this case, following parameters previously used in literature, we assume an operating frequency of 4.28 GHz and an applied magnetic field of 1600 Gauss, for which μ obtains the values $\mu = 14\mu_0$ and $\kappa = 12.4\mu_0$. The permittivity is isotropic and equal to $\epsilon_r = 15\epsilon_0$. In the presence of the magnetic anisotropy the electromagnetic equation for the infinite photonic crystal reads:

$$\nabla \times [\mu(\mathbf{r})^{-1} \nabla \times \mathbf{E}] = \epsilon(\mathbf{r})\omega^2 \mathbf{E}, \quad (2)$$

where μ is the matrix given by Eq. (1) and ϵ is scalar.

We begin by characterizing each band of the photonic crystal by calculating its Chern number. The Chern number is used to quantify the topology of the modes; it essentially characterizes the quantized global behavior of the wavefunctions on the entire dispersion band. Thus each band is characterized by

$$\begin{aligned} C_n &= \frac{1}{2\pi} \int_{BZ} \mathbf{F}_n(\mathbf{k}) d^2k = \frac{1}{2\pi} \int_{BZ} \nabla_{\mathbf{k}} \times \mathbf{A}_n(\mathbf{k}) d^2k \\ &= \frac{1}{2\pi i} \oint_{\partial BZ} \langle \mathbf{u}_{n,k} | \nabla_{\mathbf{k}} | \mathbf{u}_{n,k} \rangle d\mathbf{k}, \end{aligned} \quad (3)$$

where n is the number of the band, $\mathbf{F}_n(\mathbf{k})$ is the Berry curvature (an analogue of the magnetic field in quantum Hall systems), and $\mathbf{A}_n(\mathbf{k}) = -i \langle \mathbf{u}_{n,k} | \nabla_{\mathbf{k}} | \mathbf{u}_{n,k} \rangle$ is the Berry connection, with the Hermitian inner product defined as $\langle \mathbf{E}_1 | \mathbf{E}_2 \rangle = \int d^2r \epsilon(\mathbf{r}) \mathbf{E}_1^* \cdot \mathbf{E}_2$. Functions $\mathbf{u}_{n,k}$ correspond to the normalized periodic eigenstates that satisfy the relation $|\mathbf{u}_{n,k}(\mathbf{r})\rangle = e^{i\mathbf{k}\mathbf{r}} |\mathbf{E}_{n,k}(\mathbf{r})\rangle$ where $\mathbf{E}_{n,k}$ corresponds to the n^{th} solution, or n^{th} band, of the full wave problem formulated in Eq. (2).

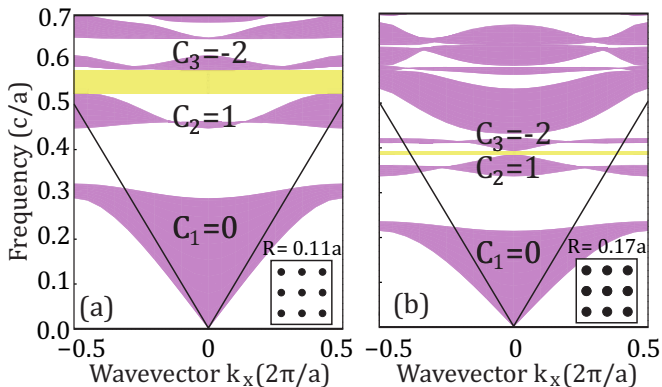


FIG. 2. Design of a magneto-optical photonic crystal supporting free space sustained topological surface states, initial step: Bringing the bandgap formed between the bands of different Chern numbers, +1 and -2, below the lightline. Projected band diagram of the magneto-optical infinite photonic crystal with constant lattice constant a and variable rod radius (filling factor): (a) $R = 0.11a$ as in Ref.15 and (b) $R = 0.17a$. Yellow areas denote the bandgap between band 2, $C_2 = +1$, and band 3, $C_3 = -2$. Black lines indicate the light cone.

As described in Ref. 15, the first step is to find a time reversal symmetric band structure (absence of external magnetic field) with a pair of photonic bands degenerate at discrete k -points which holds for $R = 0.11a$. The application of the magnetic field and the induced magnetic anisotropy lifts the degeneracies and generates bands with different Chern numbers (see Fig. S4 provided in the Supplemental Material of the document [52]). The projected band structure and the Chern number of each band for the case of $R = 0.11a$ (used in Ref. 15) are presented in Fig. 2(a). The band structures are calculated numerically by performing eigenvalues analysis in Comsol Multiphysics, imposing the proper Floquet boundary conditions. Having numerically calculated the eigenfrequency and electric field spatial distribution of each eigensolution, we apply the k -space integration of Eq. (3) and calculate the Chern number for each band. The first band is characterized by Chern number $C_1 = 0$, the second by $C_2 = +1$, and the third by $C_3 = -2$. In contrast to the topology of the air outside the photonic crystal is trivial with the Chern number equal to zero. The band gap between the second and the third band is located properly to host a topological edge state associated with $\sum C_n \neq 0$ (and has been shown to do so). To enable the emergence of a topological surface state capable of coupling to evanescent decaying solutions in free space, it is necessary that the hosting bandgap lies below the lightline. In contrast to the interface between two photonic crystals where this is easily accomplished by choosing the band structures and photonic band gaps, here this has to be accomplished by lowering the bandgap of the topological photonic crystal relative to the lightline in vacuum and is achieved by increasing the filling factor (radius of the rods). Figure 2(b) presents the projected band diagram and the Chern number of the photonic crystal with $R = 0.17a$. As shown in Fig. 2(b), there is no change in the Chern numbers of the lowest three bands, $C_1 = 0$, $C_2 = +1$, and $C_3 = -2$, upon adjusting the radius of the rods, while the bandgap between bands 2 and 3 now lies below the lightline.

Next we consider a finite photonic crystal and demonstrate topological plasmonic modes. Having established the geometric parameters where the infinite photonic crystal opens a bandgap below the lightline with $\sum C_n \neq 0$, we proceed with calculating the dispersion diagram in the finite photonic crystal surrounded by air that actually supports the topological surface states. In particular, we calculate the dispersion of the supported modes travelling in x -direction, i.e., parallel to the interface, assuming the supercell geometry illustrated in Fig. 1(b). Figure 3(a) shows the dispersion of the x -travelling modes in the supercell as the black dotted lines, within the wavevector range $k_x = [-0.5, 0.5]$ (normalized, in $2\pi/a$ units), assuming strict periodicity in the y -direction, $k_y = 0$. The projected band diagram of the infinite crystal is indicated by the pink shaded areas. As observed, the eigensolutions of the supercell lie within the bands of the infinite crystal, or else, correspond to bulk propagating modes. This

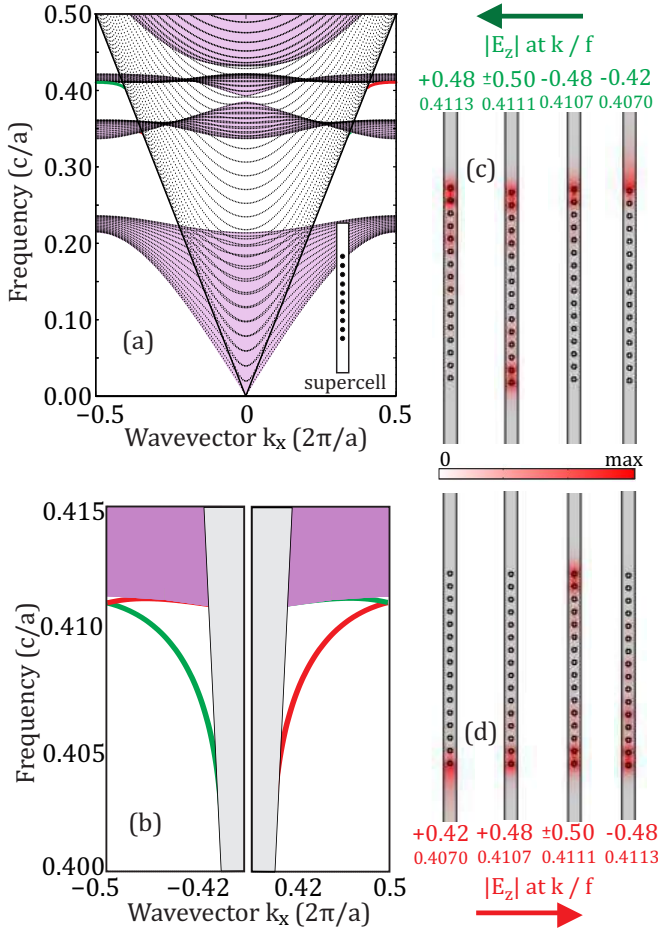


FIG. 3. The emergence of the topological plasmonic state at the termination of a truncated uncorrugated rectangular photonic crystal for the case of $R = 0.17a$. (a) Black dots: Dispersion diagram of the x -travelling modes in the supercell. Pink shaded areas: Projected band structure of the corresponding infinite photonic crystal. The solid black lines denotes the lightline. (b) Detail of (a) for $\pm k_x$ near the Brillouin zone edge, where we see the emergence of the topological surface state. Spatial distribution of the electric field (absolute) of selected eigensolutions in the green branch (c) and red branch (d) of the surface mode below band 3.

concerns all the solutions apart from a narrow area below the third band, where a slipping branch coming from the third band with Chern number $C_3 = -2$ appears (one single-sided branch each for $\pm k_x$). This branch corresponds to a mode which is propagating neither in the bulk crystal nor in the air; It is actually localized at their interface. It is interesting to observe that in this case of square photonic crystal, the free space topological mode does not cross the second and the third band as has been reported for the hexagonal case[41], but lies above the lower edge of the bulk states of the third band (see the pink shaded area of the third band around $k_x = 0$).

Figure 3(b) presents a detail of the band structure of the supercell and the infinite photonic crystal shown in Fig.3(a), focusing on frequencies just below the

third band, where the surface state emerges for $k_x = \pm[0.38, 0.5]$ and normalized $f = [0.4, 0.415]$. We observe the emergence of two branches, below the lightline and with the states below characterized by $\sum C_n \neq 0$ that cross at the edge of the Brillouin zone, $k_x = \pm 0.5$. These solutions correspond to surface modes. Figures 3(c) and 3(d) present the evolution of the spatial distribution of the absolute value $|E_z|$ of the surface mode electric field of these states as k_x varies. Notice that the solutions of the green branch appear confined only at the top part of the truncated system and the red only at the bottom part. This is a consequence (and evidence) of the unidirectionality of the surface modes. The Floquet-periodic boundaries imposed at the side edges of the supercell force the surface mode solutions travelling anticlockwise to appear only in a single side of the air terminated photonic crystal structure. Focusing on the green branch and the eigensolutions that appear on the top of the crystal, we observe that for positive k_x [right panel of Fig 3b and field distribution at $k_x = +0.48$ in Fig. 3(c)] the branch exhibits negative group velocity, $d\omega/dk < 0$, which points to $-x$ propagating modes. As the mode enters the negative k_x regime, the group velocity [points $k_x = +0.48, -0.48, -0.42$ in left panel of Fig. 3(c)], becomes positive and the mode retains its $-x$ propagation direction. The opposite behavior is observed in the red branch with modes traveling in the $+x$ direction. In all, this indicates the existence and anticlockwise propagation of the topological surface mode. At the crossing points on the edge of the Brillouin zone, $k_x = \pm 0.5$, both the branches appear with the electric field being confined both at the top and the bottom of the structure. Note that there is another, residual, surface mode solution that emerges just below the second band and very close to the light line, marked as a single spot in Fig. 3(a). This mode is extremely narrow, it emerges from the $C_2 = +1$ band but coexist with the excited bulk modes of the finite structure in the x direction.

For a physical implementation operating at 4.28 GHz, a realistic system that could sustain this topological plasmonic mode would consist of long YIG rods of radius approximately equal to $R = 4.93$ mm aligned in a square lattice with a lattice constant approximately equal to $a = 29$ mm. Notice that the rather narrow bandwidth of the surface mode of about 1.8% justifies our initial assumption for the constant material properties around the working frequency 4.28 GHz. However, μ and κ are typically chosen in the vicinity of the magnetic resonance and thus the materials parameter deviation, even in this narrow-band regime, is not absolutely negligible. In fact, the resonant dispersion leads to a further reduction of the bandwidth of the order of 1.5%. Further optimizations to increase the bandwidth, such as variable geometrical and material parameters are possible.

III. DIRECT SCATTERING DEMONSTRATION: UNIDIRECTIONALITY, BACK-SCATTERING IMMUNITY AND ROBUSTNESS

To complement the band structure and unambiguously demonstrate the unidirectional propagation of the surface state obtained at the interface of the gyrotropic/air system, we perform direct scattering simulations in Comsol Multiphysics, assuming a finite magneto optical photonic crystal composed of 15×15 rods with $R = 0.17a$ (square structure). The results are shown in Fig. 4. As illustrated in Fig. 4(a), we place a current point source, $\mathbf{j} = I_0 \mathbf{e}_z \delta(\mathbf{r} - \mathbf{r}_0)$, near the middle of the top edge, just above the finite photonic crystal structure. We excite the point source with a frequency equal to the eigensolution of the surface branch in Fig. 3(a), $f = 0.4103$ (normalized frequency). At this frequency, components of the omnidirectional point source (near-)field (consisting of a very broad spectrum of k values) couple with the free space topological surface state of the crystal, which then propagates anticlockwise around the surface of the finite photonic crystal (the corresponding energy flow is shown in Fig. S1 of the Supplemental Material document [52]).

As a topological mode, the unidirectional propagation of the surface mode is immune to defects and impurities such as the corners of the structure. Thus the surface mode passes over the corners without reflection and circulates around the structure; However, the impedance discontinuity presented by the corners still leads to leakage into free-space propagating modes at those locations. Due to the radiation losses, the wave returns to the point source attenuated in amplitude, as seen in Fig. 4(a). The panels in Fig. 4(b) and 4(c) present the scattering results for frequencies below and above the bandwidth of the topological surface mode, at normalized frequency $f = 0.4$ and $f = 0.411$, respectively. The normalized frequency $f = 0.4$ lies within the bandgap of the crystal and the radiation coming from the point source is mostly reflected by the structure (a weak coupling with the surface mode is recorded) but no propagating modes localized to the surface can be detected. The normalized frequency $f = 0.411$ lies in the third band of the crystal and the point source radiation couples with the propagating bulk modes of the third band of the crystal and hence we observe diffraction patterns within the bulk photonic crystal but again, no surface mode. It should be noted that it is the topologically induced chirality of mode that is responsible for the back-scattering-free propagation of the surface mode and its insensitivity to surface scatterers. The surface state is robust against disturbance of the surface because it is protected by the topology of the bulk photonic crystal. Also note that while topological modes sandwiched between bandgap materials are perfectly dark even around defects, here we observe some radiation as a result of being a surface mode between the photonic crystal and the vacuum. This, however, is a desired property for most applications, as it allows the

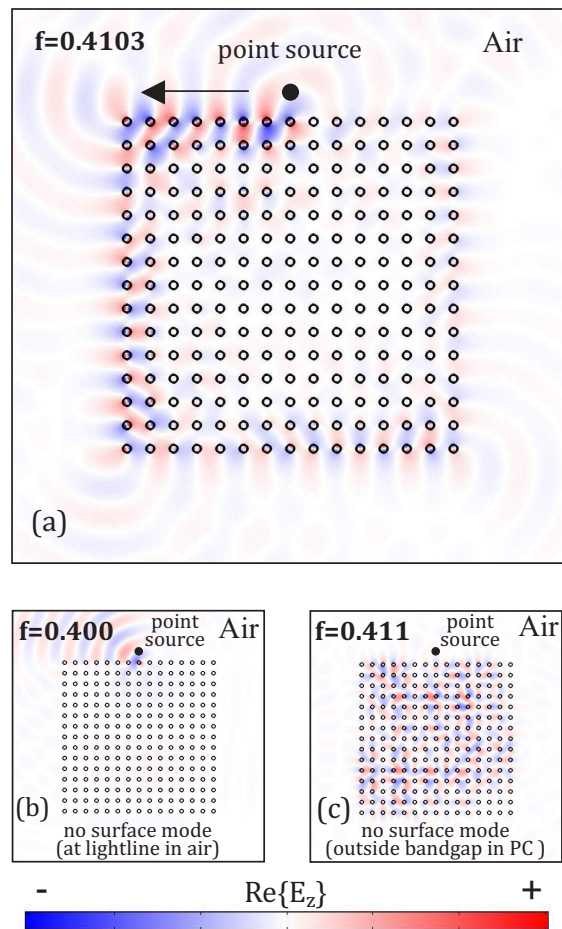


FIG. 4. Demonstration of the free space, one-way topological surface state propagating bound to the interface between the gyrotropic crystal and air at selected frequencies. (a) For a normalized frequency $f = 0.4103$, the surface state is well defined and propagates localized to the surface, anticlockwise around the circumference of the finite photonic crystal consisting of 15×15 gyrotropic rods with $R = 1.7a$. (b) For a normalized frequency $f = 0.4$, i.e., below the surface mode band, the dipole radiation is mostly reflected and no mode localized to the surface is present. (c) For a normalized frequency $f = 0.411$, i.e., above the extent of the surface mode band, the dipole radiation couples with the bulk propagating mode of the third band of the crystal and again no surface mode is present.

controlled outcoupling from the photonic crystal assisted by the topological surface mode.

Additionally, we utilize an alternative way to calculate and verify the surface mode band structure directly from the surface fields of the scattering simulation. In particular, we estimate the surface mode dispersion directly from frequency domain simulations of a finite photonic crystal by analyzing a cross-section of the surface fields along the boundary of the photonic crystal. The surface modes are excited by a remote point source and the spatial distribution of the surface fields is collected as function of frequency. To obtain cleaner results, we apodize the spatial

distribution $E_z(y)$ by an appropriate windowing function to minimize the disturbance from the corners and finite length of the sampling surface. Also, we use a sufficiently large crystal of 11×121 rods to improve the spectral resolution. We then perform a Fourier analysis (numerical FFT along the spatial dimension of the sample), where the sharp peak in the resulting Fourier spectrum then traces the surface mode dispersion in (k, ω) -space.

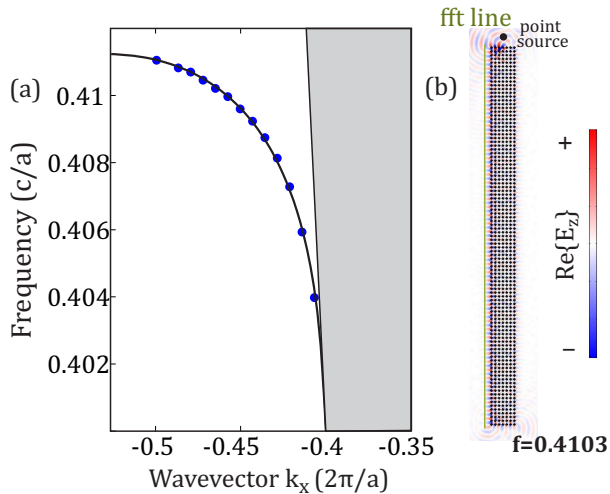


FIG. 5. Direct determination of the band structure of the chiral topological surface modes on a finite gyrotropic photonic crystal. (a) Retrieved surface mode dispersion: The blue symbols are the data points from the Fourier analysis of the surface fields, the black line the data from the supercell calculations. (b) Geometry and typical field distribution $\text{Re}\{E_z\}$ of the surface mode, excited by a $(k$ -broadband) point source in frequency domain. The green line indicates the cross-section along which the electric field is sampled for Fourier analysis.

The results are shown in Fig. 5. The left panel, Fig. 5(a), shows the retrieved dispersion of the chiral topological surface mode (blue data points) superimposed on the dispersion relation obtained from the supercell method (solid black line). The gray shaded area indicates the light cone in air. Figure 5(b) illustrates the geometry and typical field distribution $\text{Re}\{E_z\}$ of the surface mode, excited by a $(k$ -broadband) point source, where the green line indicated the path along which the fields are sampled for the Fourier analysis. The field distribution shown corresponds to a normalized frequency of $f = 0.4103$. We find excellent agreement between the two methods. The direct, Fourier analysis method avoids the need of "unwrapping" the usually quite complicated supercell band diagram and gives directly physically intuitive results. Thus it is shown, that the direct frequency-domain scattering method to obtain the surface mode dispersion is an excellent, nearly foolproof way to cross-check the surface mode band structure. In the Supplemental Material [52], in Fig. S4 we demonstrate a comparison of the retrieval approach in topologically trivial against a non-trivial free space surface states [37, 53],

which further supports the efficiency of the the direct frequency-domain scattering method to obtain the surface mode dispersion.

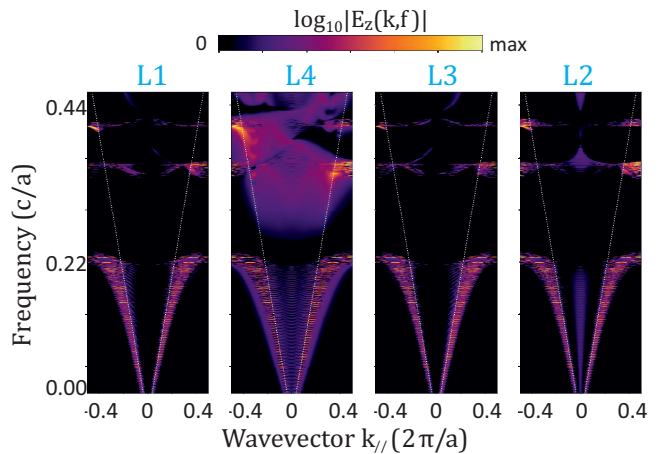


FIG. 6. Full dispersion relation retrieved from the Fourier analysis of the electric field along the edges L1 (left edge), L4 (top edge), L3 (right edge), and L2 (bottom edge), around the circumference of an 61×61 rods finite photonic crystal, as schematically depicted in Figure 7a. The unidirectional topological surface mode (propagating counterclockwise around the photonic crystal) can be clearly seen at around $f = 0.41$, occurring only for negative $k_{||}$ near the lower edge of the third band and outside the light cone (dotted white line). Tails of the bulk modes produce the bright spots in the supercell predicted bulk frequency bands.

The Fourier analysis of the frequency-domain field distributions resulting from the scattering of a suitable delta-source provides us with the powerful tool to estimate the dispersion properties but also allows the calculations of the power flow characteristics of the surface mode in the various parts of a structure. Additionally, with the Fourier analysis we are also able to directly determine the directionality of the modes for the various branches in the dispersion relation, which is not trivial in the supercell calculation because of the additional symmetries imposed by the boundary conditions. To do so we return to a square, finite photonic crystal consisting of 61×61 gyrotropic rods, the geometry of which is illustrated in Fig. 7(a). Using a point-source located near the middle of the upper edge of the structure, we obtain the relevant scattering simulations and perform a Fourier analysis of the electric field distribution along the surface of the finite photonic crystal to calculate the surface mode dispersion relation and surface energy flow in each edge segment, i.e., L1 (left edge), L4 (top edge), L3 (right edge), and L2 (bottom edge) as schematically depicted in Fig. 7(a). The results for the full dispersion band retrieved from the FFT analysis for each edge segment are presented in Fig. 6. Both the bulk and the surface mode appear as bright traces in the dispersion diagrams (the bulk modes sustain fields along the edges where we record the fields). For orientation the lightline in air is

indicated by the dotted white line. The second panel, L4, expectedly shows the strongest field as it is closest to the point source, but also suffers the most from the superimposition of the near- and propagating field of the point source overshadowing the surface modes. We can easily identify the unidirectional topological surface mode, occurring only for negative $k_{//}$ near the lower edge of the third band and outside the light cone. The chiral surface mode associated with the lower edge of band 3, excited by the point source in the middle of the top edge L4, can be clearly traced from L1, to L2, to L3, propagating only counterclockwise around the photonic crystal and proving the unidirectionality of the mode. The direction of the propagation is inherited by the third band with Chern number $C_3 = -2$. Figure 6b, especially in panel L4, also contains a hint of a clockwise propagating chiral surface mode occurring only for positive k_x , just below the lower edge of the second band with $C_2 = +1$ and very close to the lightline. This would correspond to the analog mode seen in the supercell band structure [Fig. 3(a)] but the numerical resolution in this case is marginal at best. Nevertheless, the change from counter-clockwise propagation for the band 3 surface mode to clockwise propagation for the mode associated with band 2 would be commensurate with the change in Chern number for the two topologically nontrivial bands.

Further details of the Fourier analysis concerning the chirality/unidirectionality, robustness of the (3rd band) topological surface mode against back-scattering, and the unidirectional energy flow, attenuated only by leakage into free space propagating modes are provided in Fig. 7. As already mentioned above, Fig. 7(a) shows the setup of the FFT analysis. Figure 7(c) shows the evolution of the magnitude of the electric field, $|E_z|$, of the surface mode along the edges L1, L2 and L3 for a frequency of $f = 0.41$ (normalized). The amplitude is globally normalized by the mean value of $|E_z|$ in segment L1. We observe that the mean electric field is approximately constant in each segment as there is no material loss or back reflection at the corners, which would lead to the appearance of standing wave patterns. We note that this refers in particular for the mean value since the proximity to the photonic crystal rods induces sinusoidal modulation of the surface fields showing in the short-wavelength oscillations. The superposition of fringe propagating fields from source and corner leakages contributes to the minor, long-wavelength modulations, especially around the transition points from L1 to L2 and L2 and L3, corresponding to the corners of the structure and leading to the sharp local peaks observed in Fig. 7(b). Considering the levels of the electric field amplitude at $f = 0.41$, we observe that through the propagation in the L1 segment the mean absolute field is equal to 1 and it becomes 0.7 in the second segment L2 and 0.5 in the third corner, indicating a 70% transmission coefficient in each corner, with the remainder lost to radiation leakage, but no return loss in the surface mode. The spatial Fourier spectra along the edge segments for a fixed frequency $f = 0.41$

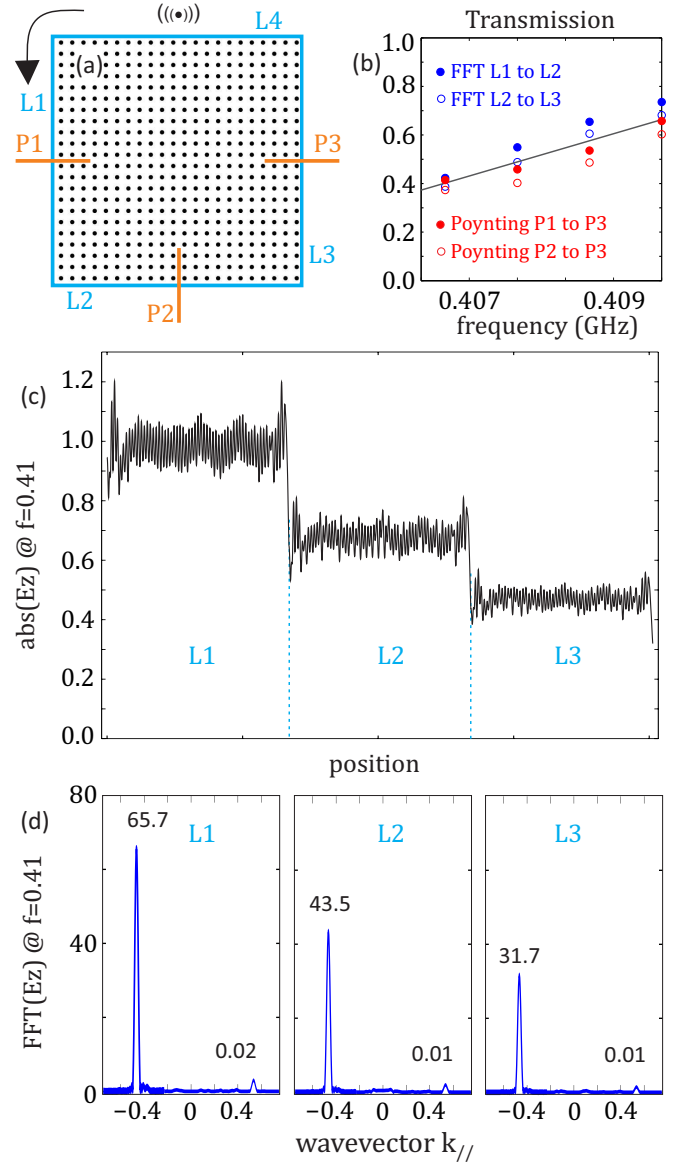


FIG. 7. (a) Finite photonic crystal structure schematic with the edges (L1-L4) along which the Fourier analysis and energy flow calculation, cross-sections P1-P3 are performed. (b) Transmission coefficient derived from the FFT data calculated along the peripheral edges L1, L2 and L3, shown in (d), for a single frequency, $f = 0.41$, in comparison to the corresponding transmission coefficient derived by calculating the energy flow through the cross-sections P1, P2 and P3. (c) The magnitude of the electric field E_z plotted at the peripheral edges L1, L2 and L3 for a frequency $f = 0.41$. (d) Spatial FFT spectra of the electric field in segments L1, L2, and L3, for $f = 0.41$, clearly showing the unidirectionality of the surface mode.

are shown in Fig. 7d. Once again we observe that we obtain only negative k solutions which is a consequence of the one-way propagation of the topological modes. Looking at segment L1 at $k = -0.465$, we record a narrow peak with magnitude 65.7. The magnitude of the FFT

at the opposite $k = +0.465$ is equal to 0.02, which translates in a practically zero reflection coefficient (the exact value is 0.03%), another proof that the topological mode has zero back-scattering. Note that there are also some small peaks in other k values which is a consequence of the coexisting free space radiating fields that are generated in the corners (and the source). Similar reflection values are calculated for segments L2 and L3. To calculate the transmission from segment L1 to segment L2 we obtain the ratio between the intensity of the peak in the FFT analysis at the point $k = -0.465$. Thus, for frequency $f = 0.41$, the power transmitted from segment L1 to segment L2 is equal to 70%. Since there are no material losses, the remaining power is radiated through the L1L2 corner. Analog we calculate a similar radiation loss percentage in the corner L2L3. Alternatively we can calculate the transmission and radiation loss in each corner by calculating the energy flow through the cross-sections P1, P2, and P3 shown in the schematic shown in Fig. 7(a). Figure 7(b) presents the spectral evolution of the transmission and radiation loss calculated by the FFT analysis (blue points) and the power flow calculations (red points) as a function of the frequency. Some small discrepancies are attributed to the finite size of the structures and cross-sections, the possible contribution of bulk fields, etc. We observe the tendency that for higher frequencies we obtain higher transmission in the segments and, therefore, lower radiation loss in the corners, which is a consequence of the surface mode's decreasing wavelength and increasing confinement to the photonic crystal surface (this tendency can be seen also in Fig. 5).

IV. CONCLUSIONS

We have shown the emergence of topological, unidirectional surface states at the interface of finite, simple square lattice, gyrotropic photonic crystals with air, elim-

inating the need for an outside photonic material to enable chiral surface modes. We demonstrated the chirality and dispersion of the surface state in supercell band structure calculations and by direct scattering of a point source from a finite photonic crystal. Our study revealed a unidirectional topological plasmonic state which propagates anticlockwise around the finite photonic crystal, unaffected by defects and back-scattering. The scattering study in particular allowed for an independent measurement of the surface state dispersion not relying exclusively on supercell calculations and proved that the direct frequency-domain scattering method to obtain the surface mode dispersion is an excellent, nearly foolproof way to cross-check the surface mode band structure. In contrast to buried topological surface states, the observed surface modes at the photonic crystal/air interface have the advantage of being accessible to the outside world, allowing to take advantage of the defect-tolerant back-scattering-free surface modes to engineer emission from PC surfaces into arbitrary free-space beam shapes and direction.

V. ACKNOWLEDGEMENT

Work at Ames Laboratory was supported by the Department of Energy (Basic Energy Sciences, Division of Materials Sciences and Engineering) under Contract No. DE-AC02-07CH11358. Work at FORTH was supported by the European Union and Greek national funds through the Operational Program Competitiveness, Entrepreneurship and Innovation, under the call RESEARCHCREATEINNOVATE (2nd Cycle); acronym: SEMI-WEB; project code: T2EDK-02073 and the European Unions Horizon 2020 FETOPEN programmes under project VISORSURF grant agreement No. 736876 and NANOPOLY grant agreement No. 829061.

-
- [1] X.-L. Qi and S.-C. Zhang, Topological insulators and superconductors, *Rev. Mod. Phys.* **83**, 1057 (2011).
 - [2] L. Lu, J. Joannopoulos, and M. Soljai, Topological photonics, *Nat. Photon.* **8**, 821 (2014).
 - [3] M. Hafezi, E. A. Demler, M. D. Lukin, and J. M. Taylor, Robust optical delay lines with topological protection, *Nat. Phys.* **7**, 907 (2011).
 - [4] M. Hafezi, S. Mittal, J. Fan, A. Migdall, and J. M. Taylor, Imaging topological edge states in silicon photonics, *Nat. Photon.* **7**, 1001 (2013).
 - [5] Y. Yang, Y. Yamagami, X. Yu, P. Pitchappa, J. Webber, B. Zhang, M. Fujita, T. Nagatsuma, and R. Singh, Terahertz topological photonics for on-chip communication, *Nat. Photon.* **14**, 446 (2020).
 - [6] B. Bahari, A. Ndao, F. Vallini, A. El Amili, Y. Fainman, and B. Kant, Nonreciprocal lasing in topological cavities of arbitrary geometries, *Science* **358**, 636 (2017).
 - [7] M. Segev and M. A. Bandres, Topological photonics: Where do we go from here?, *Nanophotonics* **10**, 425 (2020).
 - [8] J. D. Joannopoulos, S. G. Johnson, J. N. Winn, and R. D. Meade, *Photonic crystals: Molding the flow of light* (2011).
 - [9] A. Goban, C. L. Hung, J. D. Hood, S. P. Yu, J. A. Muniz, O. Painter, and H. J. Kimble, Superradiance for atoms trapped along a photonic crystal waveguide, *Phys. Rev. Lett.* **115**, 063601 (2015).
 - [10] S. B. Hasan, A. P. Mosk, W. L. Vos, and A. Lagendijk, Finite-size scaling of the density of states in photonic band gap crystals, *Phys. Rev. Lett.* **120**, 237402 (2018).
 - [11] J. C. Stephens, G. Rosenzweig, M. A. Shapiro, R. J. Temkin, J. C. Tucek, and K. E. Kreischer, Subterahertz

- photonic crystal klystron amplifier, *Phys. Rev. Lett.* **123**, 244801 (2019).
- [12] C. P. Mavridis, A. C. Tasolamprou, S. B. Hasan, T. Koschny, E. N. Economou, M. Kafesaki, C. M. Soukoulis, and W. L. Vos, Local density of optical states in the three-dimensional band gap of a finite photonic crystal, *Phys. Rev. B* **101**, 235309 (2020).
- [13] F. D. M. Haldane and S. Raghu, Possible realization of directional optical waveguides in photonic crystals with broken time-reversal symmetry, *Phys. Rev. Lett.* **100**, 013904 (2008).
- [14] S. Raghu and F. D. M. Haldane, Analogs of quantum-hall-effect edge states in photonic crystals, *Phys. Rev. A* **78**, 033834 (2008).
- [15] Z. Wang, Y. D. Chong, J. D. Joannopoulos, and M. Soljačić, Reflection-free one-way edge modes in a gyromagnetic photonic crystal, *Phys. Rev. Lett.* **100**, 013905 (2008).
- [16] Z. Wang, Y. Chong, J. Joannopoulos, and M. Soljai, Observation of unidirectional backscattering-immune topological electromagnetic states, *Nature* **461**, 772 (2009).
- [17] K. von Klitzing, The quantized hall effect, *Rev. Mod. Phys.* **58**, 519 (1986).
- [18] W.-J. Chen, S.-J. Jiang, X.-D. Chen, B. Zhu, L. Zhou, J.-W. Dong, and C. T. Chan, Experimental realization of photonic topological insulator in a uniaxial metacrystal waveguide, *Nat. Commun.* **5** (2014).
- [19] S. Weimann, M. Kremer, Y. Plotnik, Y. Lumer, S. Nolte, K. G. Makris, M. Segev, M. C. Rechtsman, and A. Szameit, Topologically protected bound states in photonic paritytime-symmetric crystals, *Nat. Mater.* **16**, 433 (2017).
- [20] M. Proctor, X. Xiao, R. V. Craster, S. A. Maier, V. Giannini, and P. A. Huidobro, Near-and far-field excitation of topological plasmonic metasurfaces, *Photonics* **7**, 81 (2020).
- [21] P. E. Stamatopoulou, V. Yannopapas, N. A. Mortensen, and C. Tserkezis, Manipulating the photonic hall effect with hybrid mie-exciton resonances, *Phys. Rev. B* **102**, 195415 (2020).
- [22] F. R. Prudencio and M. G. Silveirinha, First principles calculation of topological invariants of non-hermitian photonic crystals, *Commun. Phys.* **3**, 221 (2020).
- [23] M. Wang, R.-Y. Zhang, L. Zhang, D. Wang, Q. Guo, Z.-Q. Zhang, and C. T. Chan, Topological one-way large-area waveguide states in magnetic photonic crystals, *Phys. Rev. Lett.* **126**, 067401 (2021).
- [24] L.-H. Wu and X. Hu, Scheme for achieving a topological photonic crystal by using dielectric material, *Phys. Rev. Lett.* **114**, 223901 (2015).
- [25] S. Peng, N. J. Schilder, X. Ni, J. van de Groep, M. L. Brongersma, A. Alù, A. B. Khanikaev, H. A. Atwater, and A. Polman, Probing the band structure of topological silicon photonic lattices in the visible spectrum, *Phys. Rev. Lett.* **122**, 117401 (2019).
- [26] G. G. Pyrialakos, N. Schmitt, N. S. Nye, M. Heinrich, N. V. Kantartzis, A. Szameit, and D. N. Christodoulides, Symmetry-controlled edge states in the type-ii phase of dirac photonic lattices, *Nat. Commun.* **11** (2020).
- [27] M. Proctor, M. Blanco de Paz, D. Bercioux, A. Garcia-Etxarri, and P. Arroyo Huidobro, Higher-order topology in plasmonic kagome lattices, *Appl. Phys. Lett.* **118**, 091105 (2021).
- [28] M. Parto, Y. G. N. Liu, B. Bahari, M. Khajavikhan, and D. Christodoulides, Non-hermitian and topological photonics: Optics at an exceptional point, *Nanophotonics* **10**, 403 (2020).
- [29] C. Coulais, R. Fleury, and J. van Wezel, Topology and broken hermiticity, *Nat. Phys.* **17**, 9 (2021).
- [30] Y.-X. Xiao, K. Ding, R.-Y. Zhang, Z. H. Hang, and C. T. Chan, Exceptional points make an astroid in non-hermitian lieb lattice: Evolution and topological protection, *Phys. Rev. B* **102**, 245144 (2020).
- [31] A. Bergman, R. Duggan, K. Sharma, M. Turand, A. Zadok, and A. Alu, Observation of anti-parity-time-symmetry, phase transitions and exceptional points in an optical fibre, *Nat. Commun.* **12**, 486 (2021).
- [32] A. C. Tasolamprou, L. Zhang, M. Kafesaki, T. Koschny, and C. M. Soukoulis, Experimentally excellent beaming in a two-layer dielectric structure, *Opt. Express* **22**, 23147 (2014).
- [33] A. C. Tasolamprou, L. Zhang, M. Kafesaki, T. Koschny, and C. M. Soukoulis, Frequency splitter based on the directional emission from surface modes in dielectric photonic crystal structures, *Opt. Express* **23**, 13972 (2015).
- [34] C. W. Hsu, B. Zhen, A. D. Stone, J. D. Joannopoulos, and M. Soljačić, Bound states in the continuum, *Nat. Rev. Mater.* **1**, 16048 (2016).
- [35] A. C. Tasolamprou, T. Koschny, M. Kafesaki, and C. M. Soukoulis, Near-infrared and optical beam steering and frequency splitting in air-holes-in-silicon inverse photonic crystals, *ACS Photonics* **4**, 2782 (2017).
- [36] M. Scaravilli, A. Micco, G. Castaldi, G. Coppola, M. Gioffr, M. Iodice, V. La Ferrara, V. Galdi, and A. Cusano, Excitation of bloch surface waves on an optical fiber tip, *Adv. Opt. Mater.* **6**, 1800477 (2018).
- [37] A. C. Tasolamprou, L. Zhang, E. N. Economou, C. M. Soukoulis, and T. Koschny, Surface states on photonic crystals as hybrid dielectric metasurface bound states of the termination layer, *ACS Photonics* **7**, 2842 (2020).
- [38] E. N. Economou, Surface plasmons in thin films, *Phys. Rev.* **182**, 539 (1969).
- [39] X. Ao, Z. Lin, and C. T. Chan, One-way edge mode in a magneto-optical honeycomb photonic crystal, *Phys. Rev. B* **80**, 033105 (2009).
- [40] Y. Poo, R.-x. Wu, Z. Lin, Y. Yang, and C. T. Chan, Experimental realization of self-guiding unidirectional electromagnetic edge states, *Phys. Rev. Lett.* **106**, 093903 (2011).
- [41] M. Kim and J. Rho, Quantum hall phase and chiral edge states simulated by a coupled dipole method, *Phys. Rev. B* **101**, 195105 (2020).
- [42] G.-G. Liu, P. Zhou, Y. Yang, H. Xue, X. Ren, X. Lin, H.-X. Sun, L. Bi, Y. Chong, and B. Zhang, Observation of an unpaired photonic dirac point, *Nat. Commun.* **11** (2020).
- [43] P. Zhou, G.-G. Liu, Y. Yang, Y.-H. Hu, S. Ma, H. Xue, Q. Wang, L. Deng, and B. Zhang, Observation of photonic antichiral edge states, *Phys. Rev. Lett.* **125**, 263603 (2020).
- [44] R.-C. Shiu, H.-C. Chan, H.-X. Wang, and G.-Y. Guo, Photonic chern insulators made of gyromagnetic hyperbolic metamaterials, *Phys. Rev. Materials* **4**, 065202 (2020).
- [45] A. Poddubny, A. Miroshnichenko, A. Slobozhanyuk, and Y. Kivshar, Topological majorana states in zigzag chains of plasmonic nanoparticles, *ACS Photonics* **1**, 101 (2014).

- [46] L. Lin, S. Kruk, Y. Ke, C. Lee, and Y. Kivshar, Topological states in disordered arrays of dielectric nanoparticles, *Phys. Rev. Research* **2**, 043233 (2020).
- [47] A. Tripathi, S. Kruk, Y. Shang, J. Zhou, I. Kravchenko, D. Jin, and Y. Kivshar, Topological nanophotonics for photoluminescence control, *Nanophotonics* **10**, 435 (2021).
- [48] Y. Zhang, R. P. H. Wu, L. Shi, and K. Fung, Second-order topological photonic modes in dipolar arrays, *ACS Photonics* **7**, 2002 (2020).
- [49] D. Pan, R. Yu, H. Xu, and F. J. Garcia De Abajo, Topologically protected dirac plasmons in a graphene superlattice, *Nat. Commun.* **8**, 1243 (2017).
- [50] Y. Lumer and N. Engheta, Topological insulator antenna arrays, *ACS Photonics* **7**, 2244 (2020).
- [51] D. M. Pozar, *Microwave engineering* (Wiley, New York, 1998).
- [52] *See Supplemental Material at URL for more details regarding the energy flow of the topological plasmonic mode around the corners of the structure, the bulk band structure and a comparison of topologically trivial and non-trivial free space surface states in finite square photonic crystals.*
- [53] A. C. Tasolamprou, L. Zhang, E. N. Economou, C. M. Soukoulis, and T. Koschny, Theoretical and experimental investigation of the emergence of surface states on photonic crystals as hybrid dielectric metasurface bound states of the termination layer, in *2020 Fourteenth International Congress on Artificial Materials for Novel Wave Phenomena (Metamaterials)* (2020) pp. 54–56.